(Received 31 May 2025, Accepted 1 July 2025, Scheduled 11 July 2025)

A Compact Wideband MIMO Antenna Design for 5G

Tianchu Yang*, Shanhua Yao, and Xiaorong Qiu

School of Electrical and Information Engineering, Anhui University of Science and Technology, Huainan 232001, China

ABSTRACT: In this paper, a novel multiple-input multiple-output (MIMO) antenna for 5G applications in n77, n78, n79, and 6 GHz bands is proposed. The antenna structure is compact, measuring $30 \times 50 \times 1.5\,\text{mm}^3$. The antenna is composed of two microstrip antenna units, which are formed of two hexagonal rings with lotus and small human, with the floor partially removed. The antenna functions in a frequency range of 3.3 to 8.7 GHz. The flow of coupling currents is impeded, and the isolation of the antenna is improved by the use of stepped rectangular slots and the floor of the projecting T-shaped structure, resulting in the antenna having an isolation of less than -20 dB over the entire operating bandwidth. Furthermore, the envelope correlation coefficient (ECC) is less than 0.008, the diversity gain (DG) greater than 9.95, the total active reflectance coefficient (TARC) less than -30 dB, and the channel capacity loss (CCL) less than 0.32 bit/s/Hz. The simulations and measurements of the antenna demonstrate its reliability and stability, thus indicating its potential for significant applications in 5G wireless communications.

1. INTRODUCTION

In the current trends of communication technology development, 5G communication has been widely deployed and adopted due to its advantages of high speed, low latency, and large capacity. As the core component of electromagnetic wave transceivers in communication networks, antennas play a crucial role in ensuring signal transmission, network coverage, and multi-device cooperative communication. Consequently, 5G antenna design has become a research hot spot in the field of communications. Although millimeter-wave (mm Wave) technology offers significant bandwidth advantages, its large-scale commercial deployment is hindered by substantial propagation losses, insufficient omnidirectional coverage, and high equipment costs. Therefore, current research efforts are primarily focused on designing and optimizing sub-6 GHz antennas for 5G applications. Most existing 5G communication systems operate in the n77 (3.3–4.2 GHz), n78 (3.3–3.8 GHz), and n79 (4.4–5 GHz) frequency bands. In 2023, China's Ministry of Industry and Information Technology (MIIT) allocated the 6 GHz band (6.4–7.1 GHz) for 5G deployment [1], providing additional spectrum resources to alleviate spectrum scarcity and enhance network capacity and performance. With the increasing volume of user data, the adoption of MIMO technology has become essential. The channel capacity of MIMO systems scales linearly with the minimum number of antennas at the transmitter and receiver. Without requiring additional spectrum, MIMO enables simultaneous transmission and reception of multiple data streams over the same wireless channel [2], significantly improving signal diversity, transmission rates, and link reliability. However, antenna design is challenged by the mutual coupling between antenna elements and spatial correlation effects [3]. Article [4] proposed a closed-form expression for estimating the average user channel capacity of spread spectrum MIMO systems under Rayleigh fading, providing a theoretical tool for practical system design.

In recent years, planar antennas for 5G wireless communications and MIMO systems have been extensively investigated. Several innovative designs have been reported in the literature [5–14], employing specially-shaped radiating patches to achieve operation within 5G frequency bands. Ref. [5] introduced a crescent-shaped radiating patch formed by subtracting two non-concentric circles, achieving an operational bandwidth of 3.5–11 GHz, though with limited port isolation below -17 dB. The work in [6] presented a novel flower-shaped patch antenna composed of four rotationally symmetric concentric ellipses, demonstrating a broad bandwidth of 3.08–11.5 GHz but similarly suffering from moderate isolation performance (< -15 dB). A compact tri-band loop antenna was proposed in [7], featuring resonant frequencies at 2.4 GHz, 3.5 GHz, and 5.5 GHz; however, the design neither employed MIMO techniques nor achieved miniaturization (36 mm $\times$ 39 mm). The flag-shaped radiator in [8] exhibited a 2.3–5.6 GHz bandwidth, yet isolation remained below -18 dB. A circular floral fractal antenna was developed in [9], demonstrating six distinct resonances at 1.79 GHz, 3.84 GHz, 7.34 GHz, 9.08 GHz, 11.44 GHz, and 14.6 GHz, though limited to single-element implementation without MIMO configuration. A pentagonal microstrip antenna in [10] achieved tri-band operation at 4 GHz, 7 GHz, and 9.6 GHz, but with a relatively large footprint (30 mm $\times$ 54 mm). The hexagonal fractal antenna in [11] provided dual-band resonance at 2.5 GHz and 5.7 GHz, though again restricted to monopole operation. Lastly, [12] reported a frog-inspired antenna covering 3.05–13.8 GHz, yet isolation performance remained below -17 dB. Ref. [13] employed a regular octagonal radiating patch to achieve a bandwidth of 3.7–11 GHz, but the isolation is only -15 dB. In [14], the radiating patch consists of a small horizontal ellipse and two larger el-

* Corresponding author: Tianchu Yang (2023200724@aust.edu.cn).

lipses intersecting at 60° with a shared center point, achieving an antenna bandwidth of 4.3–15.36 GHz; however, the maximum antenna gain is only 5.35 dBi.

Recent studies [15–21] have systematically investigated ground plane modification techniques using parasitic elements to enhance port isolation in MIMO antenna systems. The research demonstrates that while parasitic patch implementations effectively improve isolation characteristics, inherent design trade-offs exist between performance metrics and physical dimensions. Specifically, [15] achieved a 4–10 GHz operational bandwidth through a fence-shaped parasitic patch configuration, though with a moderate isolation of −19 dB. Similarly, the T-shaped ground patch implementation in [16] yielded a 3.25–7.12 GHz bandwidth while maintaining −17 dB isolation. A more complex approach employing four centrally symmetric rectangular strips was presented in [17], yet the isolation performance remained limited to −15 dB. Notably, [18] demonstrated superior isolation below −27 dB via an interconnecting rectangular strip between ground sections, albeit with a substantially larger 64 mm × 96 mm footprint. Alternatively, the dual L-shaped ground patch configuration in [19] effectively suppressed coupling currents to achieve −19 dB isolation, while requiring a 36 mm × 53 mm board area. Ref. [20] employed parasitic elements integrated with metamaterials to achieve antenna isolation and decoupling, resulting in an isolation level below −22 dB. However, the gain is only 5.5 dBi, and the radiation efficiency is merely 0.7. Ref. [21] introduced a racket-shaped ultra-wideband MIMO antenna that utilized a T-shaped ground plane for isolation, achieving an isolation level of −20 dB, but the radiation efficiency is only 0.74. Ref. [22] presented an antenna incorporating a fork-shaped isolation structure, yet the isolation level was only −17 dB.

Recent studies [23–28] have explored ground plane slotting techniques as an effective approach to reduce current coupling between ports in antenna systems. The implementation of two concentric annular slots in the ground plane [23] achieved enhanced isolation of −20 dB, albeit with a relatively large form factor of 50 mm × 65 mm. Ref. [24] introduced a stepped T-shaped slot configuration at the ground plane's base, which successfully altered current distribution patterns but yielded only −15.5 dB isolation. More significant improvement was demonstrated in [25], where dual circular slots positioned beneath the radiating patches substantially suppressed inter-port coupling, resulting in exceptional −28 dB isolation, though requiring a 50 mm × 76 mm footprint. An alternative droplet-shaped slot design in [26] effectively redirected current paths to attain −25 dB isolation while maintaining a 50 mm × 50 mm dimension. Ref. [27] proposed a fractal snowflake-symmetric MIMO antenna incorporating a centrally truncated slot ground structure at the bottom, achieving an isolation level below −22.5 dB. However, the antenna exhibits relatively large dimensions of 32 mm × 64 mm. In [28], T-shaped and I-shaped slot structures were implemented on the ground plane, obtaining an isolation level of −30 dB, but the radiation efficiency was only 0.75–0.97. However, these studies collectively exhibit several limitations, including suboptimal physical dimensions, absence of MIMO implementation, restricted operational bandwidth, and potential for further isolation enhancement, suggesting opportunities for future optimization in antenna design methodologies.

Building upon these existing solutions, this paper proposes a novel wideband MIMO antenna structure and design methodology specifically tailored for 5G band applications, featuring an operational bandwidth of 3.3–8.7 GHz that fully covers n77, n78, n79, and 6 GHz frequency bands. The antenna features an innovative structural design, yielding superior performance parameters. The innovative design incorporates hexagonal radiators on the substrate's top layer, each embedded with circular slots and centrally positioned unique parasitic elements — a lotus-shaped patch and an anthropomorphic patch — to ensure optimal performance across 5G frequency bands. The ground plane integrates a sophisticated decoupling structure comprising stepped rectangular slots, an inverted T-shaped slot configuration, and a complementary T-shaped parasitic patch, achieving remarkable port isolation below −20 dB throughout the operational bandwidth. Extensive evaluations demonstrate the antenna's exceptional performance in key 5G broadband applications, exhibiting superior gain characteristics, excellent directional radiation patterns, ultra-low ECC, and minimal CCL, making it an ideal solution for advanced MIMO communication systems.

2. SINGLE-ELEMENT ANTENNA DESIGN

2.1. Antenna Structure

In this paper, a compact wideband MIMO antenna design for 5G is proposed for 5G applications in n77, n78, n79 and 6 GHz bands. The antenna is fabricated using a substrate with dimensions of 22 mm × 30 mm and a thickness of 1.5 mm, which is made of standard FR4 material with a dielectric constant (ε_r) of 4.4 and a loss angle tangent ($\tan\delta$) of 0.02. The front of the substrate incorporates a square hexagonal radiator and a rectangular microstrip feeder with a circular slot etched in the centre of the radiator. It also features a lotus-shaped patch and a small human-shaped patch embedded to allow free radiation of the antenna signal. The rear of the substrate features a partial base plate and a rectangular slot, which are designed to enhance the impedance matching of the antenna. Figure 1 shows the form factor of the designed antenna, where $\theta 1$ is 45°; $\theta 2$ is 30°; and $\theta 3$ is 20°. The structural dimensions of the designed antenna are shown in Table 1.

2.2. Stages of Antenna Design Evolution

The evolution of the antenna's design is delineated in six stages, as illustrated in Figure 2. In the first step, according to Equations (1)–(4), a rectangular microstrip antenna is obtained as shown in Figure 2(a). The velocity of light in air (c), frequency (f), the length of the patch (L), its width (w), the thickness of the substrate (h), and the effective dielectric constant of the dielectric (ε_r) are all taken into account in these equations. As demonstrated in Figure 3, the antenna generates a narrow bandwidth within the low 5G frequency band and exhibits resonance at the 5G frequency point of 3.8 GHz. In the second step, a triangle is excised from each side below the rectangular patch,

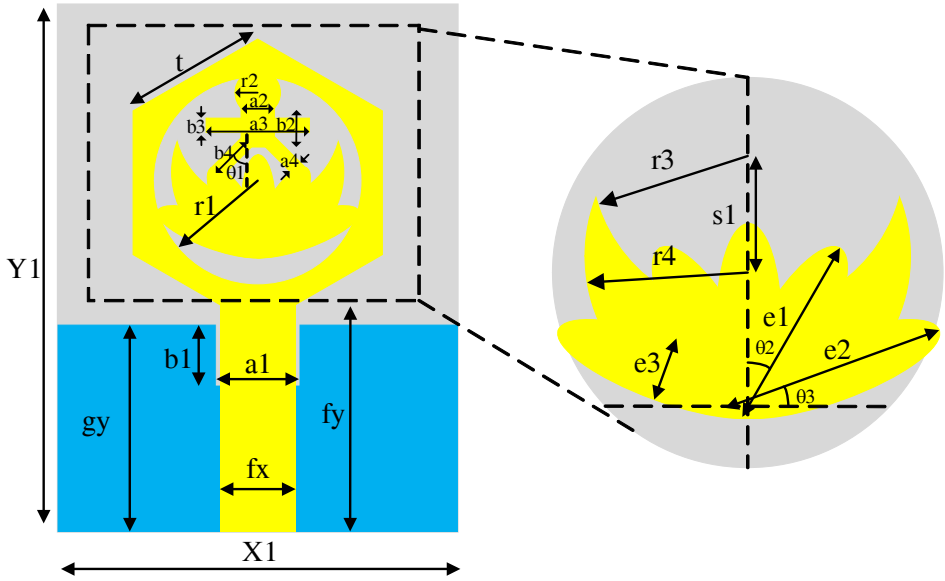

FIGURE 1. Single-element antenna structure.

TABLE 1. Dimensions of single-element antenna structures.

Parameters	**X1**	**Y1**	**fx**	**fy**	**gy**	**a1**	**a2**	**a3**	**a4**	**b1**	**b2**
Value (mm)	22	30	4	13.3	12.5	4	1.7	6	0.55	3.5	2.4
Parameters	**b3**	**b4**	**t**	**s1**	**r1**	**r2**	**r3**	**r4**	**e1**	**e2**	**e3**
Value (mm)	0.7	2.5	7.9	2.5	5.6	1.3	4.5	4.5	3	3.5	1

and an isosceles triangle is added at the top to form a positive hexagonal patch. The antenna depicted in Figure 2(b) is obtained, thereby significantly expanding the bandwidth of the antenna, yet maintaining a single resonance point. In the third step, the antenna depicted in Figure 2(c) is obtained by excavating a circle within the positive hexagonal patch, thereby forming a positive hexagonal ring. The radius of the circle is calculated and verified by Equations (5)–(7). At this juncture, the antenna exhibits two discrete resonance points. In the fourth step, a lotus-shaped patch is incorporated within the positive hexagonal ring, and the lotus consists of a crescent shape, three ellipses with an axis ratio of 3 at an angle of 30°, and two ellipses with an axis ratio of 3.5 at an angle of 140°, in order to obtain the antenna shown in Figure 2(d). The bandwidth of the antenna is increased, and one of the resonance points of the antenna is made to lie in the 6 GHz band. In the fifth step, the antenna depicted in Figure 2(e) was obtained by the addition of a small human patch situated above the lotus flower. The humanoid configuration consists of a circular patch serving as the head, a rectangular patch with width equal to the chord length of the circular patch forming the torso, an orthogonally positioned rectangular patch acting as the arms, and two rectangular strips inclined at 45° relative to the vertical axis constituting the legs. The enhanced current path has been demonstrated to expand the bandwidth. In the sixth step, slots were cut into the floor to improve the impedance matching, and the antenna shown in Figure 2(f) was obtained.

$$L = \frac{c}{2f\sqrt{\varepsilon_{eff}}} - 2\Delta L \tag{1}$$

$$\Delta L = 0.412h\frac{(\varepsilon_{eff}+0.3)\left(\frac{w}{h}+0.262\right)}{(\varepsilon_{eff}-0.258)\left(\frac{w}{h}+0.813\right)} \tag{2}$$

$$\varepsilon_{eff} = \frac{\varepsilon_r+1}{2} + \frac{\varepsilon_r-1}{2}\left(1+\frac{12h}{w}\right)^{-\frac{1}{2}} \tag{3}$$

$$w = \frac{\lambda_0}{2}\left(\frac{\varepsilon_r}{2}\right)^{-\frac{1}{2}} \tag{4}$$

$$R = T\left[1+\frac{2h}{\pi T\varepsilon_r}\left(\ln\left(\frac{\pi T}{2h}\right)+1.7726\right)\right]^{-\frac{1}{2}} \tag{5}$$

$$T = \frac{8.719\times10^9}{\sqrt{\varepsilon_r}F_{rc}} \tag{6}$$

$$F_{rc} = \frac{c}{2\pi R\sqrt{\varepsilon_{eff}}} \tag{7}$$

As illustrated in Figure 3, the final design of the antenna exhibits a bandwidth of 3.3–9 GHz, with resonance points at 3.6 GHz and 6.4 GHz.

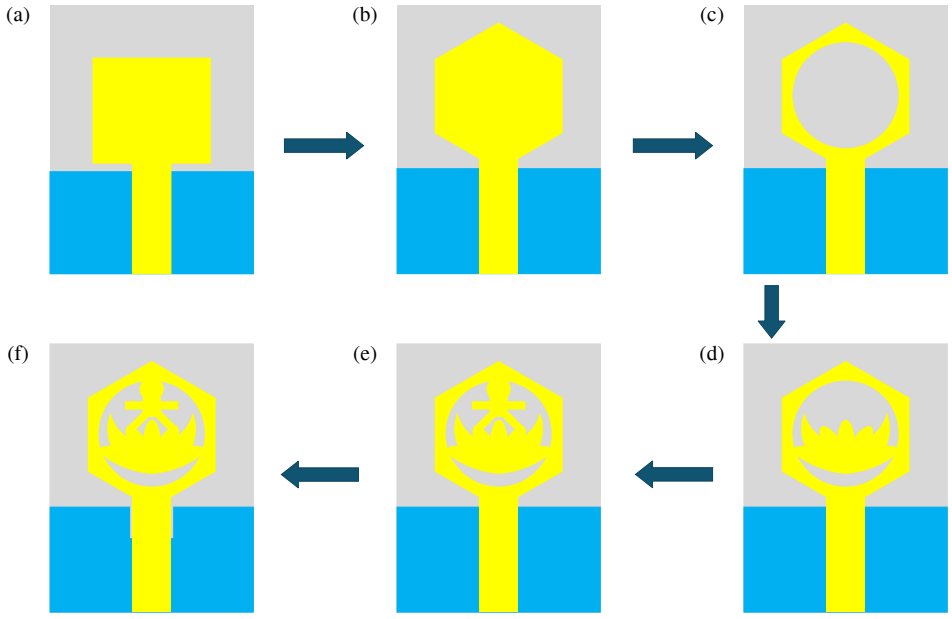

FIGURE 2. Design flow of single-element antenna: (a) Ant 1, (b) Ant 2, (c) Ant 3, (d) Ant 4, (e) Ant 5, (f) Ant 6.

TABLE 2. Dimensions of the MIMO antenna structure.

Parameters	X	Y	x1	x2	x3	x4	x5	x6	x7
Value (mm)	50	30	0.5	1	8	2.95	5.45	1	9
Parameters	x8	y1	y2	y3	y4	y5	y6	y7	
Value (mm)	1.5	2	1.5	1	9	8.5	17.4	0.1	

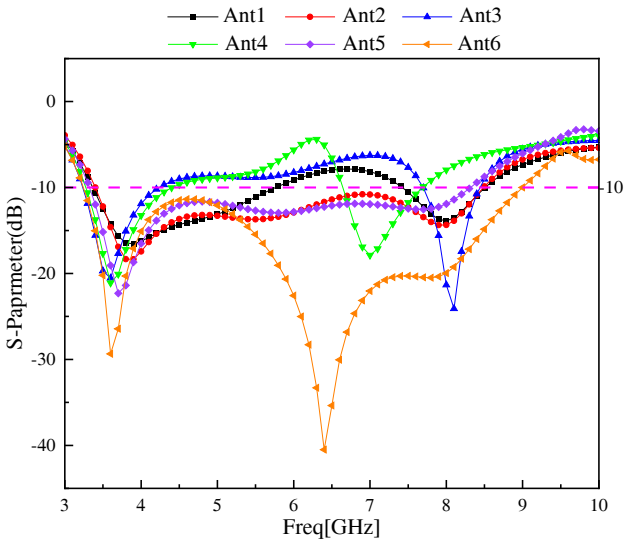

FIGURE 3. Simulation results of six antennas.

2.3. Antenna Parameter Analysis

The height gy of the floor and the width $a1$ of the rectangular slot of the floor have a significant effect on the performance of the antenna, and HFSS software is used to optimize these parameters so that the antenna achieves the best possible performance. As demonstrated in Figure 4, the bandwidth of the antenna exhibits an increase and subsequent decrease with the rise of $a1$, attaining its maximum value when $a1 = 4$ mm. As demonstrated in Figure 5, the bandwidth of the antenna exhibits an increase followed by a decrease with an increase in gy, reaching its maximum value at $gy = 12.5$ mm.

3. MIMO ANTENNA DESIGN

3.1. Antenna Structure

As illustrated in Figure 6, the geometry of wideband MIMO antenna design for 5G is demonstrated. The antenna is fabricated on a substrate measuring 30 mm $\times$ 50 mm with a thickness of 1.5 mm, using standard FR-4 material. The antenna is composed of two symmetrical radiating patches on the substrate, and its feeding mechanism is realized through a microstrip line configuration. In order to enhance the isolation between the antenna ports, a stepped rectangular slot and a stepped inverted T-shaped slot were excavated into the base plate and supplemented with a T-shaped patch. The structural dimensions of the designed antenna are shown in Table 2.

3.2. Stages of Antenna Design Evolution

The shape of the floor is continuously refined to optimize the bandwidth and decoupling design of the MIMO antenna. As shown in Figure 7, the evolution of the antenna design is di-

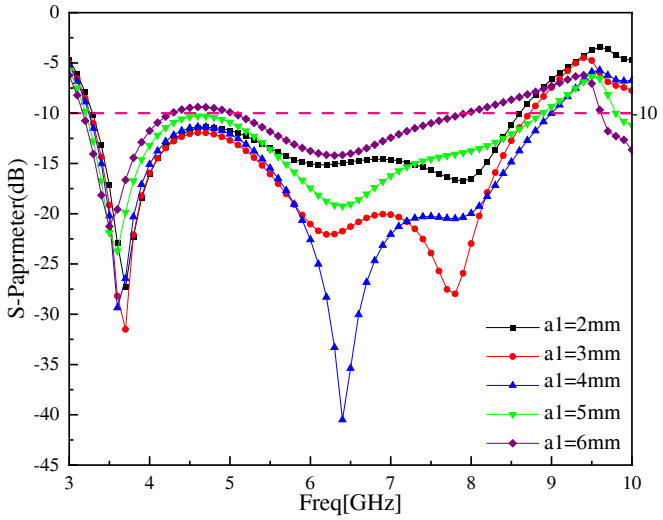

FIGURE 4. Effect of $a1$ parameter on antennas S_{11}.

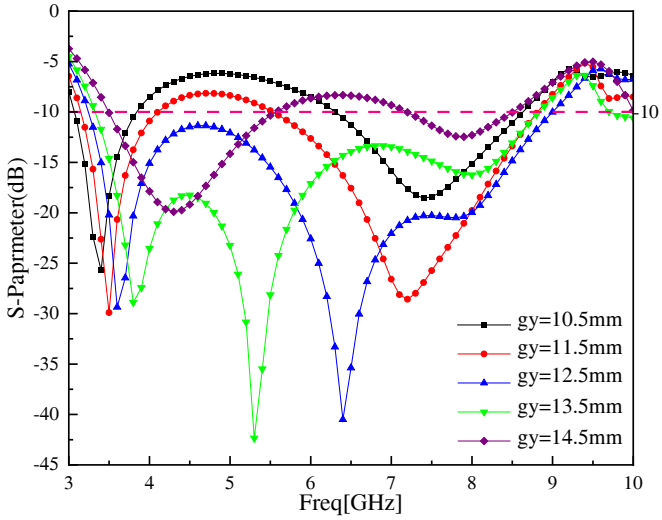

FIGURE 5. Effect of gy parameter on antennas S_{11}.

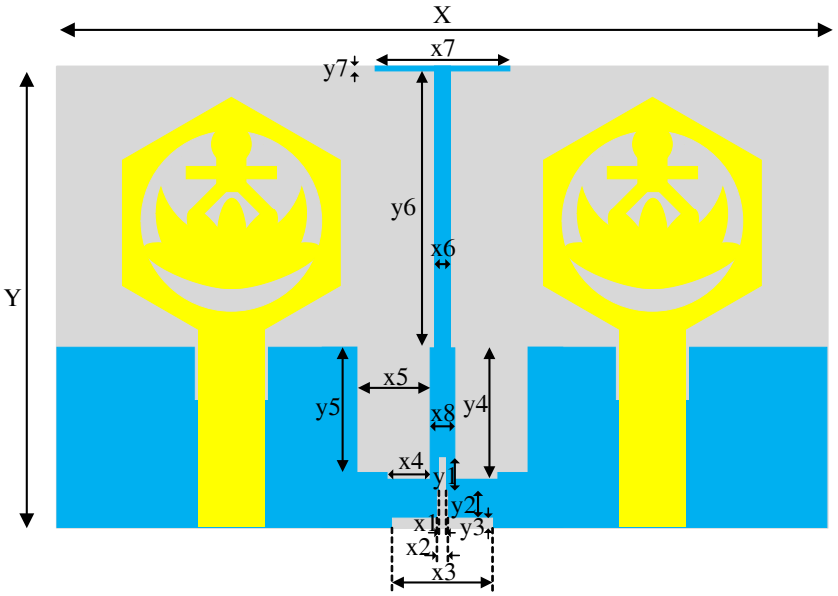

FIGURE 6. MIMO antenna structure.

vided into four stages. In the first step, the unit antenna is positioned in a symmetrical manner on both sides of the substrate, thereby resulting in the antenna depicted in Figure 7(a). At this juncture, the antenna S_{11} is situated at a level exceeding -10 dB at 4.7–5.1 GHz, and the isolation has been determined to be -12 dB. It is imperative to further reduce the coupling. In the second step, a stepped rectangular gouge treatment is taken in the middle of the floor to obtain the antenna shown in Figure 7(b). The operating bandwidth is widened, and the coupling in most of the operating bands is reduced, but the isolation remains at a level of below -12 dB. In the third step, the decoupling effect between neighboring antennas is promoted by using a T-shaped plate, and the antenna shown in Figure 7(c) is obtained. At this step, the antenna bandwidth remains largely unaltered. However, the isolation falls short of the requisite benchmark, registering at below -16 dB. This necessitates a further optimization of the antenna structure to enhance its performance. In the fourth step, a stepped inverted T-shaped gouge is made to the bottom of the floor to obtain the antenna shown in Figure 7(d). This is done in order to make the overall antenna isolation less than -20 dB. It is important to note that this is done without varying the antenna bandwidth.

The final antenna exhibits an operating bandwidth of 3.3–9 GHz, with resonance points at 3.7 GHz, 6 GHz, and 8.4 GHz, as illustrated in Figure 8(a). The antenna demonstrates an isolation rating of less than -20 dB across the entire operating bandwidth, as depicted in Figure 8(b).

3.3. Antenna Parameter Analysis

The dimensions of the stepped rectangular slot width $x5$ in the middle of the floor, the width $x6$ of the T-shaped plate, and

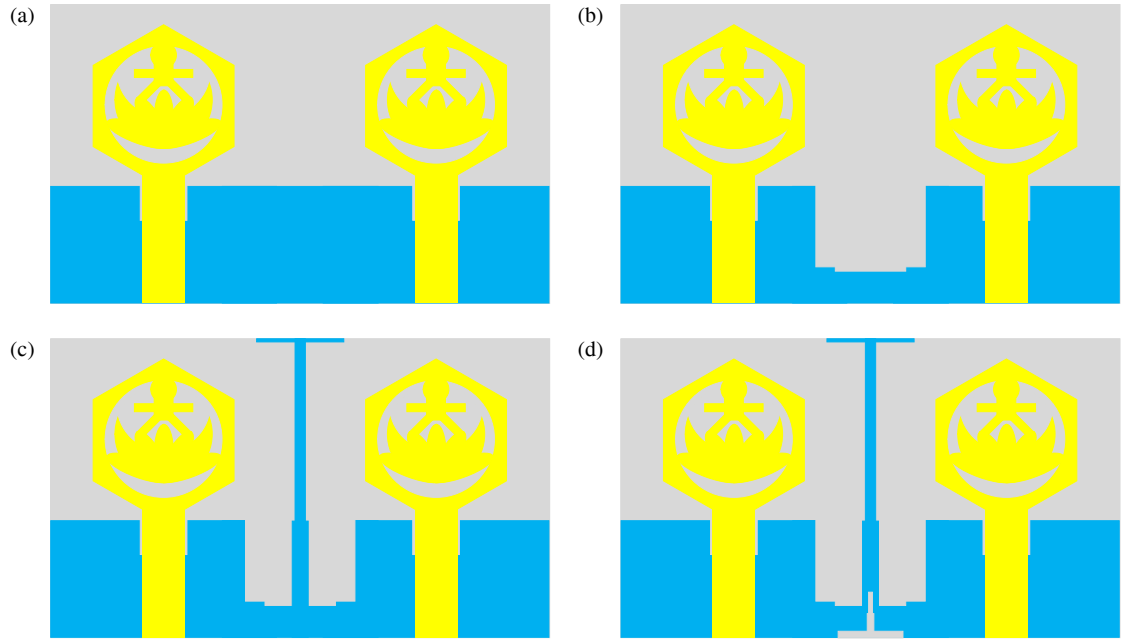

FIGURE 7. Design flow of MIMO antenna: (a) Ant I, (b) Ant II, (c) Ant III, (d) Ant IV.

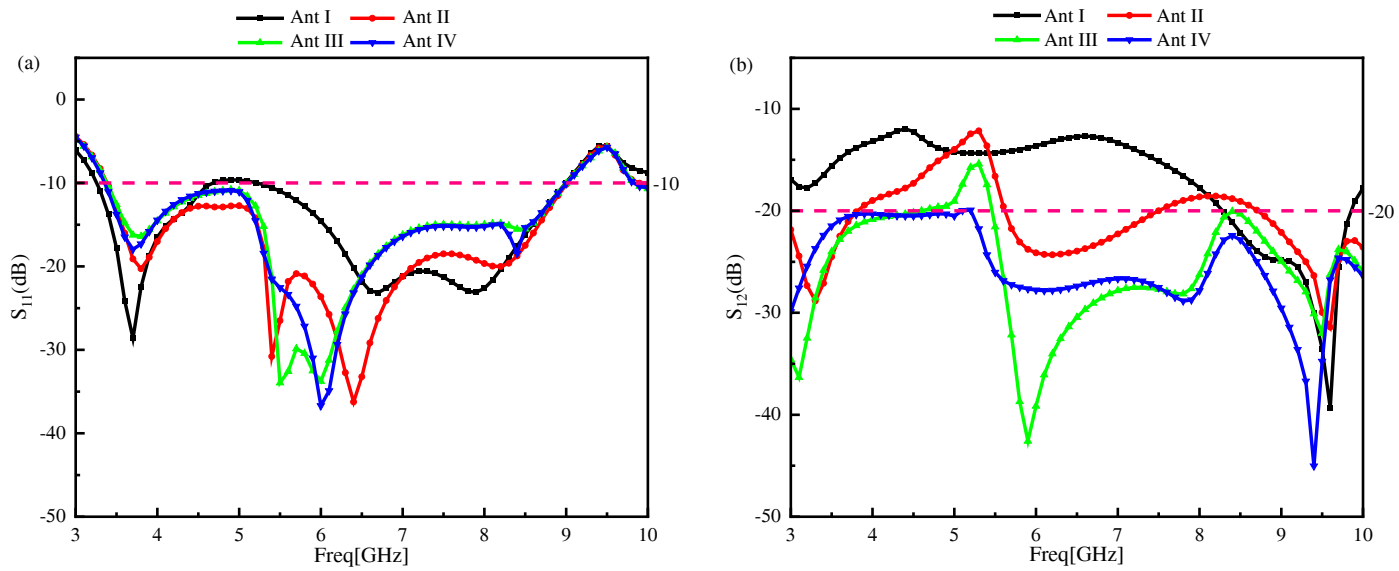

FIGURE 8. Simulation results of four antennas: (a) S_{11}, (b) S_{12}.

the length $x7$ at the top have a significant effect on the antenna performance. These parameters were optimized using HFSS software to achieve the best performance of the antenna. As demonstrated in Figure 9(a) and Figure 9(b), the antenna bandwidth initially increases and subsequently decreases with the rise in parameter $x5$, and the isolation degree also increases and then decreases. It can be concluded that the antenna exhibits an enhanced operating bandwidth and isolation decoupling at the $x5$ value of 5.45 mm. As demonstrated in Figure 10(a) and Figure 10(b), both the antenna bandwidth and isolation degree initially increase and subsequently decrease with the rise of parameter $x6$. The antenna performance attains its optimal state when the value of $x6$ is designated as 1 mm. As demonstrated in Figure 11(a) and Figure 11(b), the operating bandwidth of the antenna is observed to increase with an increase in the value of parameter $x7$. However, the isolation degree initially increases and subsequently decreases. It is evident that the antenna exhibits optimal operating bandwidth and isolation degree when the value of $x7$ is 9 mm.

3.4. Antenna Current Analysis

Figure 12 illustrates the surface current distributions of four antennas. The purpose is to enhance the decoupling performance of the MIMO antennas by analyzing their surface currents. As depicted in Figure 12(a), a rectangular patch links the ground

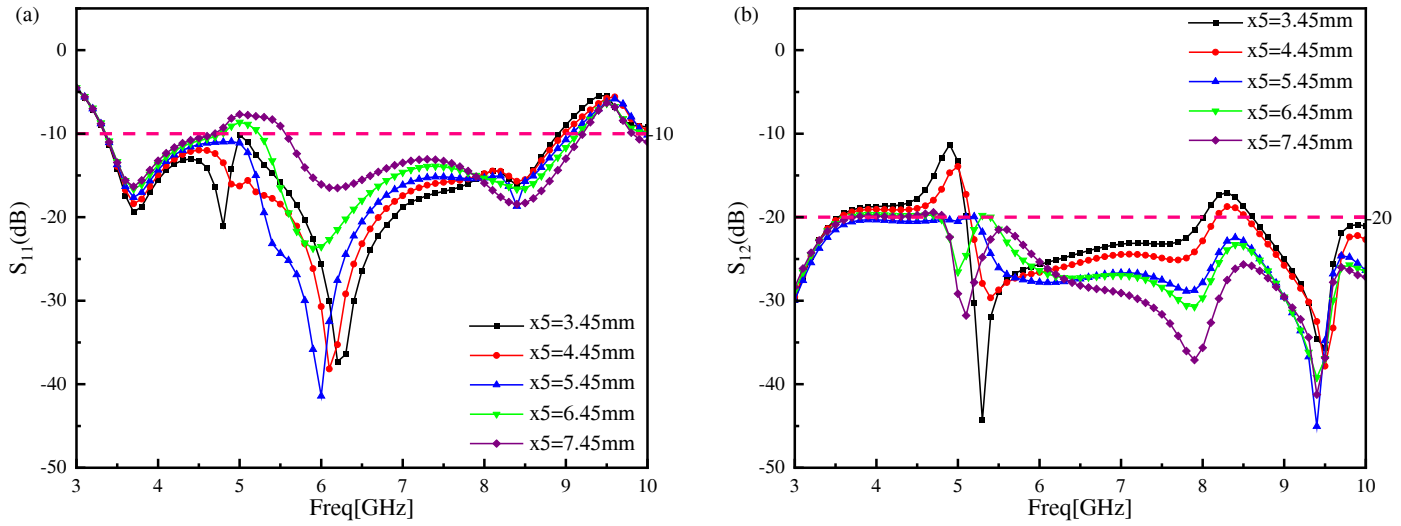

FIGURE 9. Effect of $x5$ parameter on antennas S_{11} and S_{12}: (a) S_{11}, (b) S_{12}.

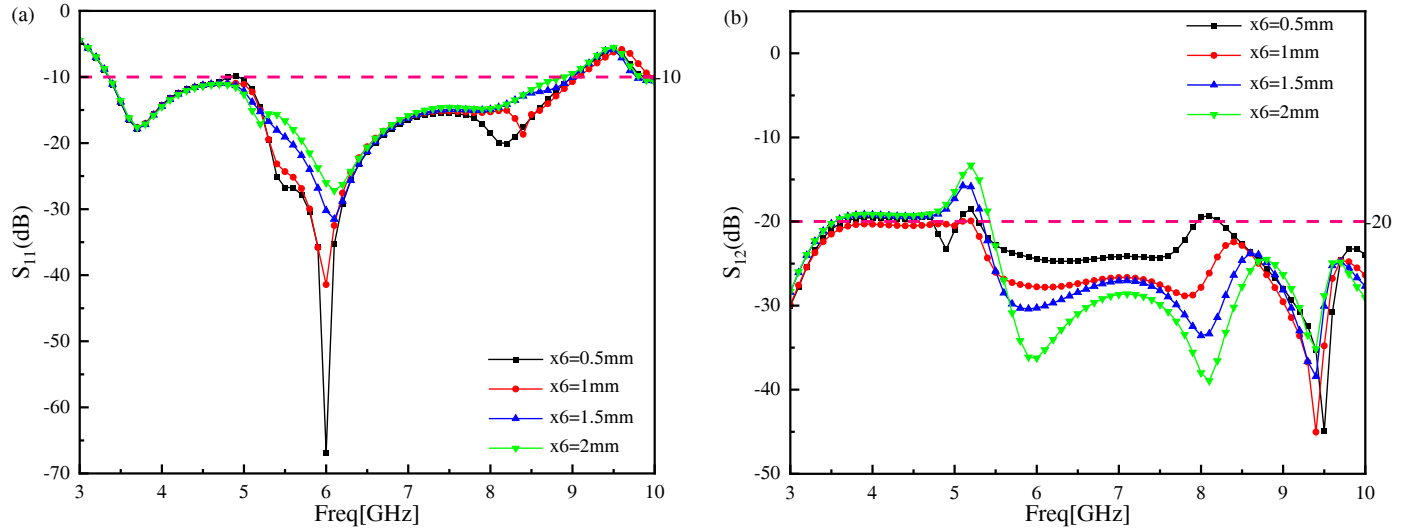

FIGURE 10. Effect of $x6$ parameter on antennas S_{11} and S_{12}: (a) S_{11}, (b) S_{12}.

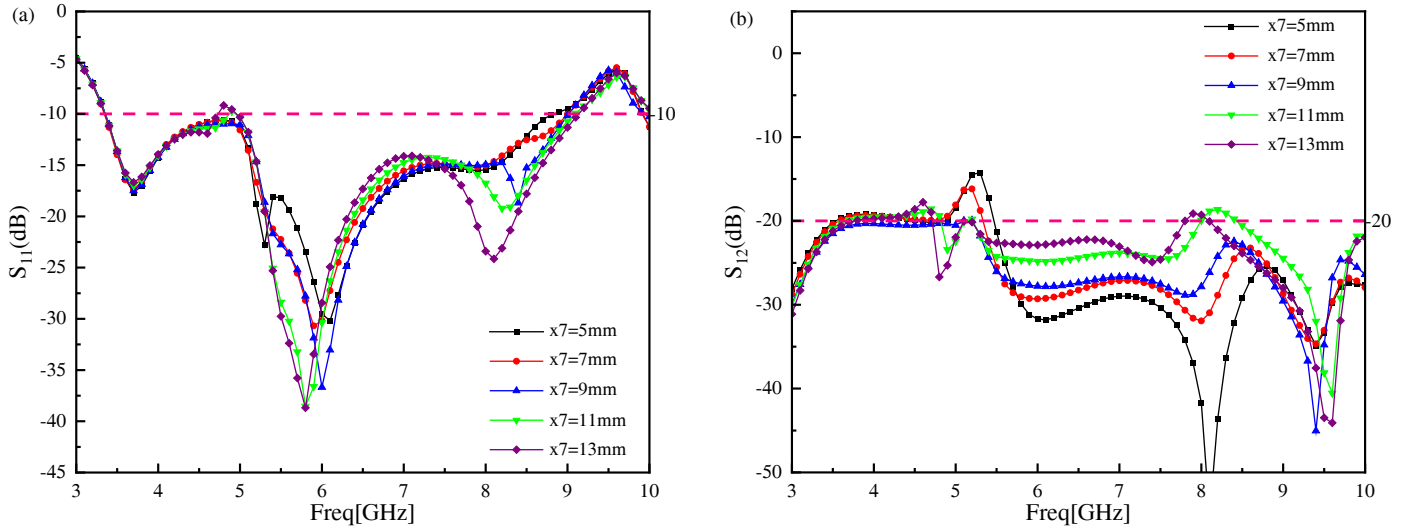

FIGURE 11. Effect of $x7$ parameter on antennas S_{11} and S_{12}: (a) S_{11}, (b) S_{12}.

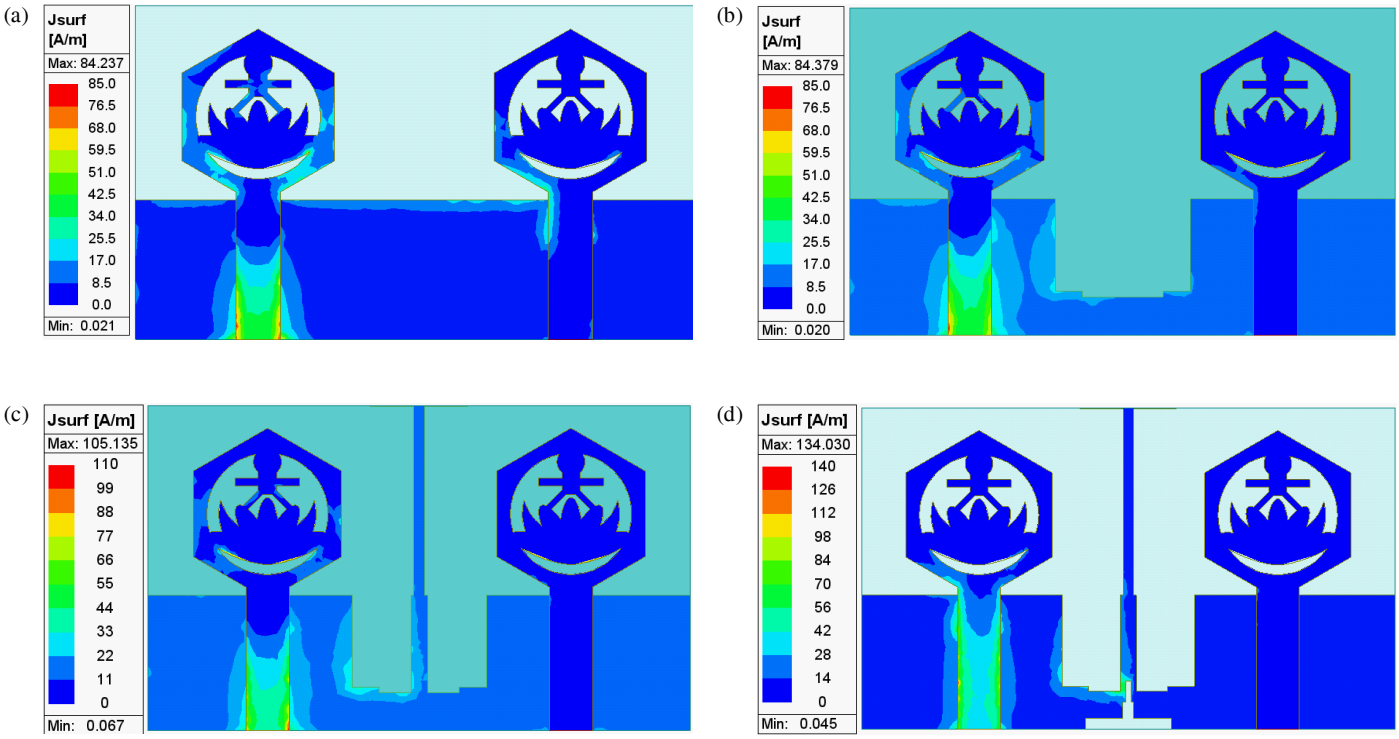

FIGURE 12. Surface currents of four floor-structured antennas: (a) Ant I, (b) Ant II, (c) Ant III, (d) Ant IV.

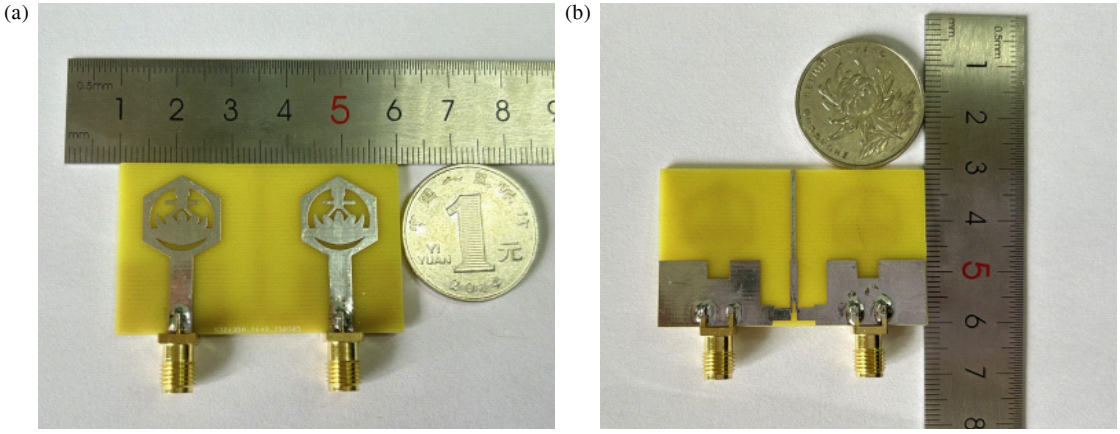

FIGURE 13. MIMO antenna fabrication prototype: (a) Front of the antenna, (b) back of the antenna.

planes of two single-element antennas, creating a new defective ground plane. The antenna is excited at Port 1. Simulations conducted using ANSYS HFSS software reveal that a significant amount of current couples to Port 2. In Figure 12(b), a stepped rectangular groove is introduced. Most of the current is blocked, and only a small amount of current couples to Port 2. For Figure 12(c), a T-shaped ground plane is employed. Although a large amount of current is present on the isolation structure, there is still a relatively small amount of coupled current at Port 2. In Figure 12(d), a stepped inverted T-shaped groove is utilized. The current at Port 2 is minimized, with almost no coupled current, indicating an optimized isolation and decoupling effect. Consequently, the isolation and decoupling structure shown in Figure 12(d) is ultimately adopted for the antenna. This structure effectively blocks the current coupling between ports, achieving the best isolation performance.

4. RESULTS AND DISCUSSION

4.1. S-Parameters

The proposed wideband MIMO antenna design for 5G was simulated using ANSYS HFSS software. To validate its practical performance, a physical prototype was fabricated based on the antenna model, with the fabricated prototype depicted in Figure 13. Antenna testing was conducted using a Siglent SNA6032A vector network analyzer, and the measurement setup is illustrated in Figure 14. As shown in Figure 15, the an-

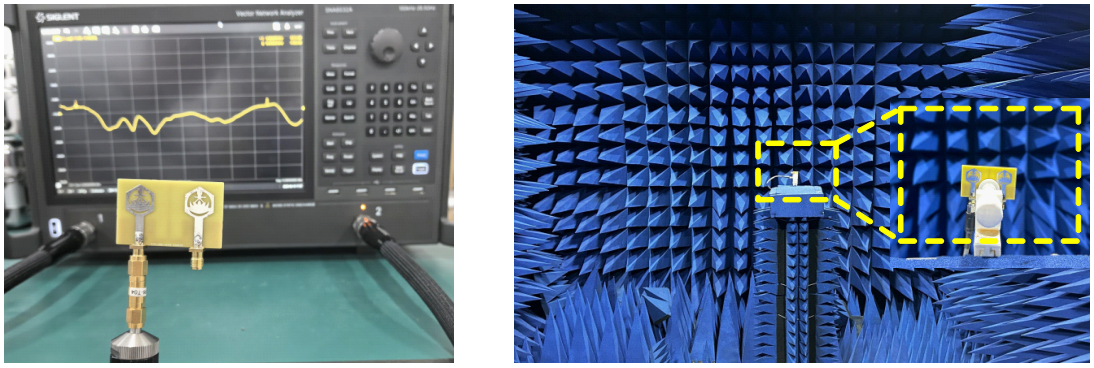

FIGURE 14. Antenna test environment.

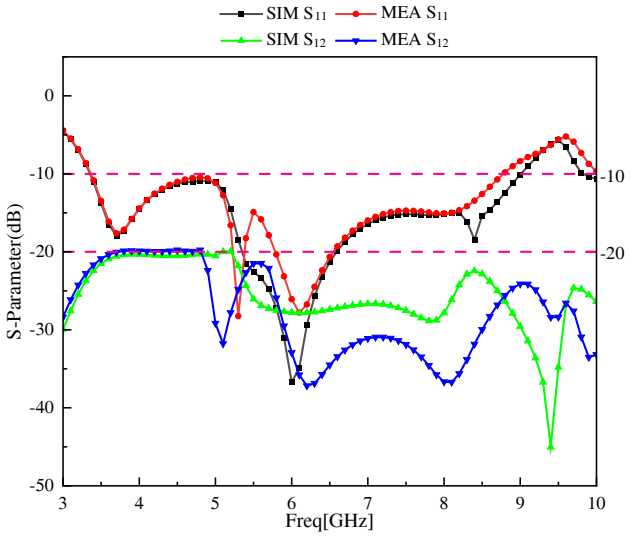

FIGURE 15. Simulated and measured S-parameters.

tenna exhibits an operational bandwidth spanning 3.3–8.7 GHz, fully covering the 5G n77 (3.3–4.2 GHz), n78 (3.3–3.8 GHz), n79 (4.4–5 GHz), and 6 GHz bands. Moreover, the measured S_{12} parameters remain below -20 dB across the entire bandwidth, demonstrating excellent port isolation. Although minor discrepancies between the simulated and measured results of S_{11} and S_{12} are observed in Figure 15, which are likely due to fabrication tolerances and test environment variations, the overall trends show strong agreement, confirming consistent antenna performance.

4.2. Radiation Properties

The radiation direction maps of the wideband MIMO antenna in the XOZ and YOZ directions were measured in a microwave anechoic chamber. Three resonance points of the antenna were selected for the measurements, and the results are shown in Figure 16. Figure 16(a) shows that the antenna achieves omnidirectional radiation in the XOZ plane at a frequency of 3.7 GHz and maximum radiation gain in the 0° and 180° directions of the YOZ plane. From Figure 16(b), it can be observed that at the frequency of 5.3 GHz, the antenna achieves the maximum radiation gain at 180° and 350° in the XOZ plane, while exhibiting nearly omnidirectional radiation characteristics in the YOZ plane. Figure 16(c) shows that the antenna achieves almost omnidirectional radiation in the XOZ plane at a frequency of 6 GHz and exhibits bidirectional radiation, achieving maximum gain in the YOZ plane at 345° and 180°. Figure 16(d) shows that the maximum radiation direction of the antenna at 8.4 GHz is distributed as follows: the XOZ plane is mainly distributed within the 330°–30° and 145°–240° intervals, while the YOZ plane is mainly distributed within the 330°–45° and 120°–190° intervals.

As illustrated in Figure 17, the maximum gain and radiation efficiency of the MIMO antenna are demonstrated. As demonstrated in Figure 17, the antenna gain is 2.5–7.1 dBi. The antenna's radiation efficiency ranges from 87% to 97%, indicating optimal radiation performance.

4.3. MIMO Antenna Performance

4.3.1. ECC and DG

Envelope correlation coefficient (ECC) refers to the correlation coefficient of signal amplitudes received by different antenna elements, serving as a parameter to evaluate the diversity performance and coupling characteristics of MIMO multi-antenna systems. A smaller ECC value indicates weaker mutual influence between antenna elements, leading to better MIMO antenna performance. Typically, for proper antenna operation, the ECC value must be less than 0.5. The ECC can be derived from Equation (8) [29]

$$\mathrm{ECC} = \frac{\left|\iint_{4\pi}\left[\vec{F}_1(\theta,\varphi) * \vec{F}_2(\theta,\varphi)\right] d\Omega\right|^2}{\iint_{4\pi}\left|\vec{F}_1(\theta,\varphi)\right|^2 d\Omega \iint_{4\pi}\left|\vec{F}_2(\theta,\varphi)\right|^2 d\Omega} \tag{8}$$

As shown in Figure 18, the maximum ECC of the proposed antenna within the operating band is approximately 0.008, demonstrating excellent decoupling capability.

Diversity gain (DG) is another key performance metric for MIMO antennas, which can be derived from the ECC. A value closer to 10 dB indicates better antenna performance. The calculation is given by Equation (9) as follows:

$$\mathrm{DG} = 10 \times \sqrt{1 - \mathrm{ECC}^2} \tag{9}$$

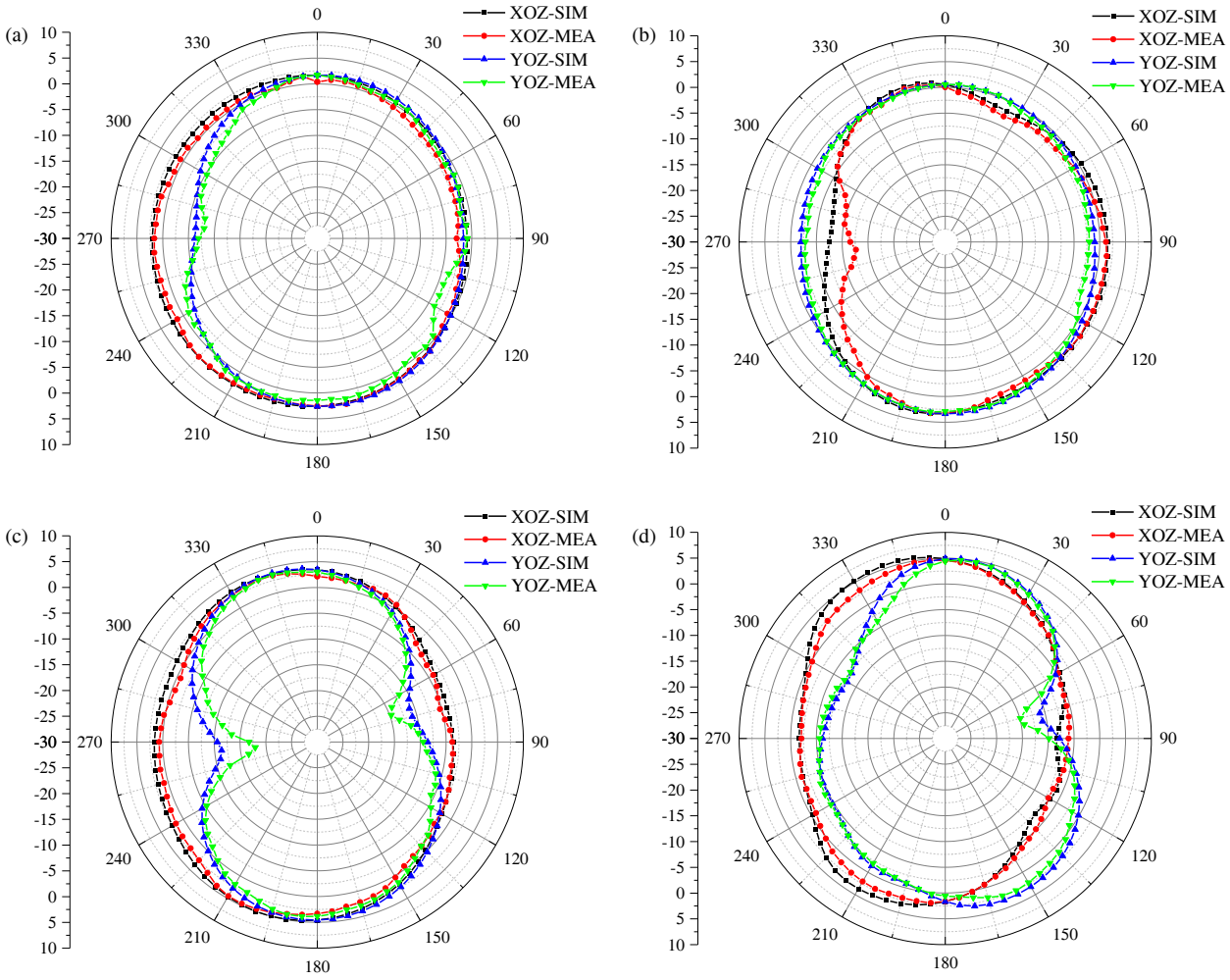

FIGURE 16. Simulated and measured orientation diagrams:(a) 3.7 GHz, (b) 5.3 GHz, (c) 6 GHz, (d) 8.4 GHz.

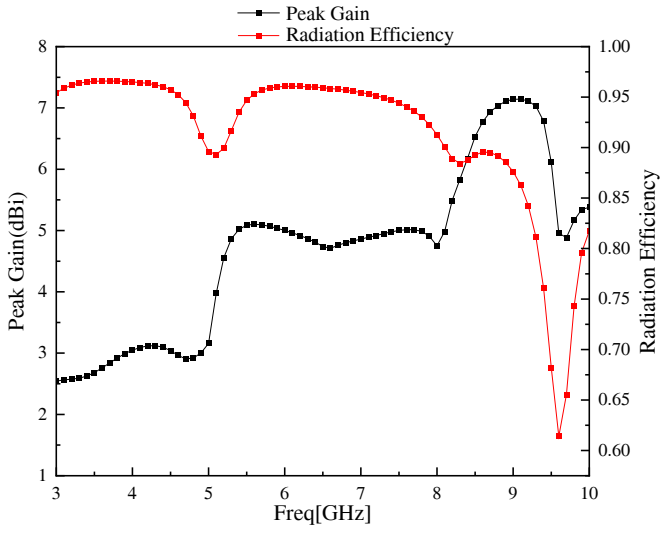

FIGURE 17. Peak gain and radiation efficiency of the antenna.

As depicted in Figure 19, the proposed antenna exhibits a minimum DG of 9.95 dB across its operational bandwidth, demonstrating superior diversity performance.

4.3.2. TARC and CCL

Total active reflection coefficient (TARC) serves as a critical performance metric for MIMO antenna systems. It characterizes the effective bandwidth of a MIMO antenna when multiple ports are simultaneously excited and can be derived from S-parameter measurements. Conventionally, a TARC value below -10 dB within the operational frequency band is considered indicative of an antenna design with low reflection loss and satisfactory phase stability. In a two-port MIMO antenna system, Equation (10) for the calculation of TARC is shown below:

$$\mathrm{TARC} = \sqrt{\frac{(S_{11}+S_{12})^2 + (S_{21}+S_{22})^2}{2}} \tag{10}$$

Figure 20 presents the TARC characteristics of the proposed antenna, demonstrating values below -30 dB across the operational frequency band. This exceptionally low reflection coefficient confirms excellent decoupling performance in the MIMO antenna system.

Channel capacity loss (CCL) represents another crucial parameter in MIMO antenna systems, quantifying the degrada-

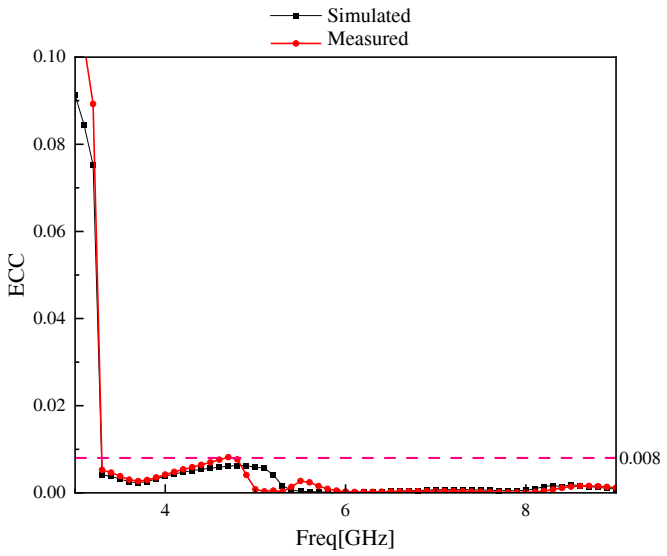

FIGURE 18. Simulating and measuring ECCs.

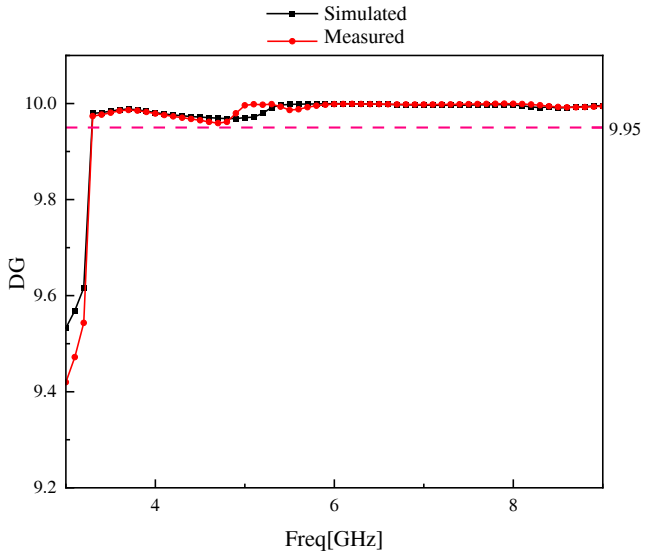

FIGURE 19. Simulating and measuring DGs.

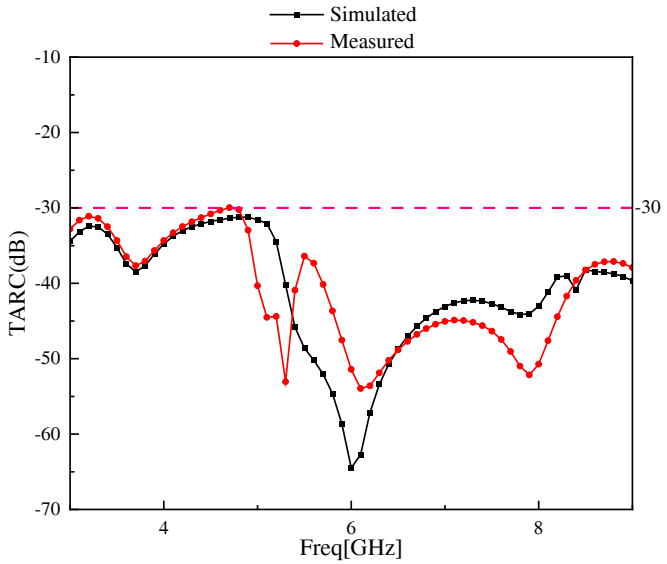

FIGURE 20. Simulating and measuring TARCs.

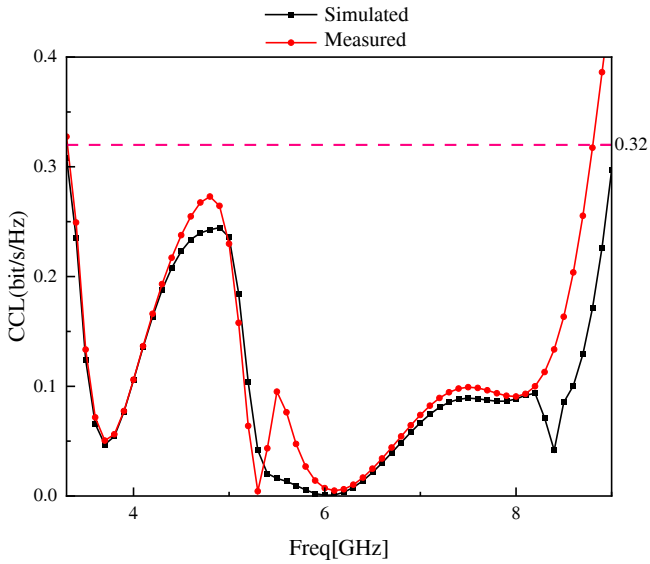

FIGURE 21. Simulating and measuring CCLs.

tion in channel capacity between antenna transceivers. The proposed design demonstrates CCL values below the 0.4 bits/s/Hz threshold throughout the operational bandwidth, meeting the acceptable performance criteria for practical implementations. The comprehensive calculation of CCL involves the coupled evaluation through Equations (11)–(14), accounting for both spatial correlation and radiation efficiency effects.

$$\mathrm{CCL} = -\log_2 \det\left(\alpha^R\right) \tag{11}$$

$$\alpha^R = \begin{bmatrix} \alpha_{11} & \alpha_{12} \\ \alpha_{21} & \alpha_{22} \end{bmatrix} \tag{12}$$

$$\alpha_{ii} = 1 - \left| \sum_{n=1}^{2} S_{in} * S_{ni} \right| \tag{13}$$

$$\alpha_{ij} = -\left| \sum_{n=1}^{2} S_{in} * S_{nj} \right| \tag{14}$$

Figure 21 presents the CCL characteristics of the proposed MIMO antenna system. The measured CCL remains below 0.32 bits/s/Hz across the entire operational bandwidth, demonstrating superior channel reliability that satisfies rigorous wireless communication requirements. This performance metric confirms the antenna's robust capability in maintaining high-quality signal transmission under MIMO operation conditions.

5. COMPARE WITH EXISTING ANTENNAS

Table 3 systematically compares the measured performance of the proposed antenna with state-of-the-art designs [13, 16, 30–36] in terms of key performance metrics including substrate

TABLE 3. Comparison of the proposed antenna with several existing antennas.

Ref	Substrate Material	Size (mm^2)	Bandwidth (GHz)	Isolation (dB)	ECC	Radiation Efficiency (%)	Gain (dBi)
[13]	FR4	16×27	3.7–11	< -15	< 0.2	40–75	6.5
[16]	FR4	25×30	3.12–7.12	< -18	< 0.005	94–97	4.2
[30]	RT/Duroid 5880	45×95	3.1–5.5	< -18	< 0.02	-	2
[31]	FR4	54×54	2.88–6.12	< -15	< 0.005	87–95	5.75
[32]	FR4	40×40	3.3–6	< -10	< 0.006	60–90	12.25
[33]	FR4	135×140	3.1–6.5	< -20	< 0.02	-	7.9
[34]	FR4	50×50.415	3.17–5.36	< -15	< 0.014	75–95	7.2
[35]	FR4	140×140	2–11.2	< -21	< 0.003	70–90	7.8
[36]	FR4	25.5×30.5	3.1–11.85	< -20	< 0.02	80–85	3.08
This Work	**FR4**	$\mathbf{30 \times 50}$	**3.3–8.7**	$\mathbf{< -20}$	$\mathbf{< 0.008}$	**87–97**	**7.1**

material, size, bandwidth, isolation, ECC, radiation efficiency, and gain. The proposed antenna exhibits superior performance across multiple dimensions. The antenna under consideration in this paper employs FR4 material as the substrate, a choice that aligns with the literature [13, 16, 31–36]. This material is notably more economical than the RT/Duroid 5880 substrate utilized in [30]. It achieves a more compact size than [30–35], demonstrates wider operational bandwidth than [16, 30–34], and shows improved isolation characteristics relative to [13, 16, 30–32, 34]. The proposed antenna achieves a lower envelope correlation coefficient (ECC) than the designs reported in [13, 30, 33, 34, 36], demonstrating superior diversity performance and reduced mutual coupling characteristics. Additionally, the design surpasses the radiation efficiency of [13, 31, 32, 34–36] and delivers higher gain than the antennas reported in [13, 16, 30, 31, 36]. These comparative results show that the proposed antenna significantly improves the overall performance with affordability, miniaturization, wide bandwidth, high isolation, low ECC, high gain, and radiation efficiency, establishing its advantages in 5G modern MIMO communication applications. The comprehensive performance improvements are attributed to the innovative design approach incorporating optimized structural parameters and effective decoupling techniques.

6. CONCLUSION

This paper presents a compact wideband MIMO antenna design for 5G, specifically targeting n77, n78, n79, and 6 GHz frequency bands. The antenna features two hexagonal radiators with rectangular microstrip feedlines on the top layer, incorporating circular slots and unique geometric elements: a lotus-shaped patch and an anthropomorphic patch embedded at the radiator centers. The ground plane employs a stepped rectangular slot and an inverted T-shaped slot configuration, complemented by a T-shaped parasitic patch to enhance port isolation, achieving consistent isolation below -20 dB across all operational bands. The proposed design demonstrates an impressive operational bandwidth from 3.3 to 8.7 GHz, fully encompassing 5G NR bands including n77 (3.3–4.2 GHz), n78 (3.3–3.8 GHz), n79 (4.4–5 GHz), and 6 GHz band (6.4–7.1 GHz). Comprehensive MIMO performance evaluation reveals outstanding diversity characteristics: an ultra-low ECC (< 0.008), high diversity gain (> 9.95 dB), exceptional TARC performance (< -30 dB), and minimal channel capacity loss (< 0.32 bits/s/Hz). These superior indicators confirm that the antenna designed in this paper has excellent performance such as high isolation and high gain in n77, n78, n79, and 6 GHz bands of 5G, which is suitable for application in the transmission of signals of the current 5G mobile networks. In the domain of antenna design, while bandwidth enhancement and high isolation represent the fundamental challenges, there are several other key issues in practical system integration, including multi-band compatibility and harmonic interference, which will be the focus of subsequent investigation.

ACKNOWLEDGEMENT

This work was partially supported by the National Natural Science Foundation of China (No. 62105004) and the Natural Science Research Program for Universities in Anhui Province (No. KJ2020A0308).

REFERENCES

[1] Ministry of Industry and Information Technology, "Regulations of the People's Republic of China on the Division of Radio Frequencies," 1–241, 2023.

[2] Molisch, A. F. and M. Z. Win, "MIMO systems with antenna selection," *IEEE Microwave Magazine*, Vol. 5, No. 1, 46–56, 2004.

[3] Paulraj, A. J., D. A. Gore, R. U. Nabar, and H. Bolcskei, "An overview of MIMO communications — A key to gigabit wireless," *Proceedings of the IEEE*, Vol. 92, No. 2, 198–218, 2004.

[4] Varzakas, P., "Average channel capacity for Rayleigh fading spread spectrum MIMO systems," *International Journal of Communication Systems*, Vol. 19, No. 10, 1081–1087, 2006.

[5] Ibrahim, A. A., M. I. Ahmed, and M. F. Ahmed, "A systematic investigation of four ports MIMO antenna depending on flexible material for UWB networks," *Scientific Reports*, Vol. 12, No. 1, 14351, 2022.

[6] Kaur, H., H. S. Singh, and R. Upadhyay, "Design and analysis of compact quad-element MIMO antenna with asymmetrical ground structures for ultra-wideband communication," *Wireless Personal Communications*, Vol. 124, No. 4, 3105–3127, 2022.

[7] Rana, S., A. K. Gautam, and S. Sharma, "Compact triple band ring shaped planar antenna for WLAN/WiMAX applications," *Wireless Personal Communications*, Vol. 139, No. 4, 2239–2251, 2024.

[8] Rekha, S., G. S. Let, S. Radha, P. Lavanya, T. Rajasekhar, and S. R. Chand, "Investigations on a compact self-isolated flag-shaped slotted MIMO antenna for triple-band applications," *International Journal of Communication Systems*, Vol. 38, No. 2, e5967, 2025.

[9] Attioui, S., A. Khabba, S. Ibnyaich, A. Zeroual, Z. Zakaria, and A. J. A. Al-Gburi, "Design of a miniaturized circular flower-shaped fractal antenna with a defected ground structure for multi-band applications," *Progress In Electromagnetics Research C*, Vol. 155, 203–211, 2025.

[10] Du, C., F. Zhang, and R. Li, "Design of tri-band flexible CPW 4-port slot MIMO antenna for conformal 5G, WIFI 6/6E and X-band applications," *Engineering Science and Technology, An International Journal*, Vol. 62, 101937, 2025.

[11] Pathak, P. A., S. L. Nalbalwar, A. E. Wagh, and J. L. Rajput, "A fractal approach to investigate SAR of HMSA UWB antenna for medical applications," *Progress In Electromagnetics Research C*, Vol. 154, 67–75, 2025.

[12] Yao, S., T. Yang, X. Qiu, and X. Li, "A frog-shaped UWB MIMO antenna design for 5G," *Progress In Electromagnetics Research C*, Vol. 151, 101–112, 2025.

[13] Dhananjeyan, R., S. Ramesh, D. R. Kumar, and O. P. Kumar, "Compact octagonal MIMO antenna system for broadband applications with enhanced isolation and wideband performance," *Scientific Reports*, Vol. 15, No. 1, 1–13, 2025.

[14] Mu, W., H. Lin, Z. Wang, C. Li, M. Yang, W. Nie, and J. Wu, "A flower-shaped miniaturized UWB-MIMO antenna with high isolation," *Electronics*, Vol. 11, No. 14, 2190, 2022.

[15] Bouba, I., L. Yang, and H. Wang, "Two element UWB-MIMO antenna with modified ground stub structure," in *2021 International Applied Computational Electromagnetics Society Symposium (ACES)*, 1–3, Hamilton, ON, Canada, 2021.

[16] Addepalli, T., "Compact MIMO diversity antenna for 5G Sub: 6 GHz (N77/N78 and N79) and WLAN (Wi-Fi 5 and Wi-Fi 6) band applications," *Wireless Personal Communications*, Vol. 132, No. 3, 2203–2223, 2023.

[17] He, L., Y. Miao, and G. Liu, "A compact 4 × 4 UWB MIMO antenna with 5G and WLAN band rejected operation," *Progress In Electromagnetics Research C*, Vol. 156, 39–47, 2025.

[18] Narayanaswamy, N. K., Y. Alzahrani, K. K. V. Penmatsa, A. Pandey, A. K. Dwivedi, V. Singh, and M. Tolani, "Machine learning aided tapered 4-port MIMO antenna for V2X communications with enhanced gain and isolation," *IEEE Access*, Vol. 13, 32 411–32 423, 2025.

[19] Yao, S., X. Qiu, and T. Yang, "A miniaturized UWB MIMO antenna design for 5G multi-band applications," *Progress In Electromagnetics Research C*, Vol. 153, 1–12, 2025.

[20] Tighilt, Y., C. Bensid, D. Sayad, S. Mekki, R. Zegadi, M. L. Bouknia, I. Elfergani, P. Singh, J. Rodriguez, and C. Zebiri, "Low-profile UWB-MIMO antenna system with enhanced isolation using parasitic elements and metamaterial integration," *Electronics*, Vol. 12, No. 23, 4852, 2023.

[21] Wang, Z., G. Song, W. Nie, M. Yang, C. Li, and M. Wang, "A racket-like UWB MIMO antenna with high isolation," *Progress In Electromagnetics Research C*, Vol. 144, 159–168, 2024.

[22] Singh, H. V. and S. Tripathi, "Compact UWB MIMO antenna with Fork-shaped stub with vias based coupling current steering (VBCCS) to enhance isolation using CMA," *AEU — International Journal of Electronics and Communications*, Vol. 129, 153550, 2021.

[23] Kansal, P., A. K. Mandpura, and N. Kumar, "Investigation of circularly polarized MIMO antenna with enhanced isolation for sub-6 GHz application," *Physica Scripta*, Vol. 99, No. 10, 105536, 2024.

[24] Pradeep, P., K. J. Sankar, and C. S. Paidimarry, "Design of a compact wideband two-port MIMO antenna for NR 5G sub-6 GHz band wireless applications," *Wireless Personal Communications*, Vol. 138, No. 2, 1193–1210, 2024.

[25] Sharma, U., G. Srivastava, M. K. Khandelwal, and P. Chaurasia, "Quad-band dual-port MIMO microstrip antenna with double integrated circularly polarized bands for 4G/5G wireless applications," *Physica Scripta*, Vol. 99, No. 9, 095544, 2024.

[26] Kaur, N., J. Kaur, and S. Sharma, "Compact wide band quad element MIMO antenna with inbuilt isolator for 5G applications," *Physica Scripta*, Vol. 100, No. 3, 035510, 2025.

[27] Mohanty, A. and B. R. Behera, "Investigation of 2-port UWB MIMO diversity antenna design using characteristics mode analysis," *AEU — International Journal of Electronics and Communications*, Vol. 124, 153361, 2020.

[28] Saxena, G., P. Jain, and Y. K. Awasthi, "High diversity gain MIMO-antenna for UWB application with WLAN notch band characteristic including human interface devices," *Wireless Personal Communications*, Vol. 112, 105–121, 2020.

[29] Sharawi, M. S., "Printed multi-band MIMO antenna systems and their performance metrics [wireless corner]," *IEEE Antennas and Propagation Magazine*, Vol. 55, No. 5, 218–232, 2013.

[30] Sandhya, A., S. Kumar, N. Radha, V. Preethi, and K. Srivastava, "Investigation of MIMO antenna design for sub-6 GHz 5G (N77/N78 and N79) applications," in *2023 International Conference on Sustainable Emerging Innovations in Engineering and Technology (ICSEIET)*, 774–777, Ghaziabad, India, 2023.

[31] Addepalli, T., R. Manda, and M. A. Kumar, "Monopole based flower-shaped 4-element MIMO antenna with high diversity performance for 4G: LTE, 5G: sub-6 GHz (n77/n78/n79), WiFi-5 and WiFi-6 bands applications," *Analog Integrated Circuits and Signal Processing*, Vol. 122, No. 1, 1–16, 2025.

[32] Doloi, T., G. S. Das, P. P. Kalita, A. Buragohain, R. Devi, and Y. Beria, "A novel 4-port MIMO antenna with chamfered edge for 5G NR n77/n78/n79 bands and WLAN applications," *Physica Scripta*, Vol. 99, No. 10, 105013, 2024.

[33] Ahmed, H., A. M. Ameen, A. Magdy, A. Nasser, and M. Abo-Zahhad, "A sub-6 GHz two-port crescent MIMO array antenna for 5G applications," *Electronics*, Vol. 14, No. 3, 411, 2025.

[34] Chidurala, S. and P. R. Amara, "Dual polarized firelight-shaped 4 Port MIMO antenna using connected defected ground for 5G Sub-6 GHz applications," *Physica Scripta*, Vol. 100, No. 6, 065534, 2025.

[35] Nawar, R. I., A. M. Abdelhady, and A. Y. Hassan, "High performance circularly polarized quad-elements for 5G wireless communications," *Arabian Journal for Science and Engineering*, 1–18, 2025.

[36] Pandya, K., T. Upadhyaya, V. Sorathiya, U. Patel, A. Pandya, and F. A. Al-Zahrani, "Highly isolated electrically compact UWB MIMO antenna for wireless communications applications," *Results in Engineering*, Vol. 24, 103082, 2024.